Infrared response of vitreous titanium dioxide films with anatase short-range order

G. Scarel
Advanced Coatings Experimental Laboratory and Materials Department, University of Wisconsin-Milwaukee, P.O. Box 784, Milwaukee, Wisconsin 53201

C. J. Hirschmugl
Department of Physics, University of Wisconsin-Milwaukee, P.O. Box 413, Milwaukee, Wisconsin 53201

V. V. Yakovlev
Department of Physics, University of Wisconsin-Milwaukee, P.O. Box 413, Milwaukee, Wisconsin 53201

R. S. Sorbello
Department of Physics, University of Wisconsin-Milwaukee, P.O. Box 413, Milwaukee, Wisconsin 53201

C. R. Aita[a)]
Advanced Coatings Experimental Laboratory and Materials Department, University of Wisconsin-Milwaukee, P.O. Box 784, Milwaukee, Wisconsin 53201

H. Tanaka and K. Hisano
Department of Applied Physics, The National Defense Academy, Yokosuka 239, Japan

(Received 12 July 2001; accepted for publication 20 October 2001)

The polarization-dependent optical response of vitreous titanium dioxide films was determined by infrared reflection–absorption spectroscopy (IRAS). The predominant nearest-neighbor coordination (short-range order) in the films was characteristic of crystalline anatase. A dielectric function $\epsilon(\nu)$ was constructed, based on random orientational disorder of anataselike, octahedral TiO_6 units relative to the substrate. This dielectric function, which is the directional average of the dielectric function for an anatase crystal in the $\mathbf{E}\perp\mathbf{c}$ and $\mathbf{E}\|\mathbf{c}$ orientations, was used to calculate energy loss functions from which theoretical IRAS spectra were obtained. Experimental absorption band frequencies are in good agreement with peaks in the calculated transverse optic loss function, $\mathrm{Im}[\epsilon(\nu)]$, at 261 and 436 cm^{-1}, and in the calculated longitudinal optic loss function, $\mathrm{Im}[-1/\epsilon(\nu)]$, at 840 cm^{-1}. Agreement (i.e., polarization-dependent behavior, band frequency, and relative intensity) between the experimental and theoretical IRAS spectra indicates that orientational disorder of TiO_6 units is the important factor governing infrared reflection–absorption behavior of the films. © *2002 American Institute of Physics.* [DOI: 10.1063/1.1427430]

I. INTRODUCTION

The behavior of titanium dioxide in response to optical photons has made this material technologically important and therefore the subject of continued study. Optical properties of TiO_2 include a wide electron energy band gap, transparency throughout the visible spectrum, and a high refractive index over a wide spectral range from the ultraviolet to the far infrared. These properties led to the use of TiO_2 for diverse thin film optical and electro-optic device applications.[1–6]

Bulk TiO_2 at atmospheric pressure and room temperature can exist in three crystalline polymorphs.[7–9] Rutile is the thermodynamically stable phase at all temperatures, while anatase and brookite form as metastable phases below ~800 °C. Titanium is in octahedral coordination with O as TiO_6 units in all polymorphs. However, different Ti–O bond length and angle, and consequently, different arrangements of TiO_6 octahedra, generate different lattice structures. The rutile and anatase lattices are tetragonal with $P4_2/mnm$ and $I4_1/amd$ space groups, respectively, and brookite is orthorhombic with $Pbca$ symmetry.[10] In addition, a series of $Ti_nO_{2n-1}(4\leqslant n\leqslant 10)$ daughter-structures form by shear operations on a rutile mother-structure to accommodate nonstoichiometry.[11]

Some bulk oxides have structural complexity, meaning (a) bond flexibility giving rise to polymorphs with the same chemistry and similar free energy of formation, and/or (b) the formation of mixed valence compounds with vernier, block, or infinitely adaptive physical structures to accommodate changes in stoichiometry.[12] A thin film grown at room temperature of such an oxide is likely to have an atomic structure in which long-range crystallographic order (LRO) is lacking, i.e., the film is noncrystalline. The precise atomic arrangement within a noncrystalline oxide film has long been the subject of discussion, and depends somewhat upon the

a)Electronic mail: aita@uwm.edu

type of structural complexity of the bulk oxide. Following Felner,[12] we classify noncrystalline oxides in terms of increasing nearest-neighbor atomic order as amorphous or vitreous. An amorphous oxide film has no short-range order (SRO), i.e., atomic coordination and chemistry at the nearest-neighbor level differ throughout the film. A vitreous oxide film has SRO, i.e., the same atomic coordination and chemistry at the nearest-neighbor level throughout the film, and furthermore, may contain ordered domains extending beyond nearest neighbors to the subnanometer or even nanometer level. In other words, a vitreous oxide film may contain nanocrystallites, but has no LRO.

Titanium dioxide meets both criteria for structural complexity, and it is not surprising that films grown at low temperature by diverse processes contain noncrystalline material, either alone or coexisting with crystalline anatase and/or rutile.[13–29] Furthermore, Eastman[30] reported a noncrystalline structure coexistent with crystalline material in freestanding nanostructured TiO_2, and astutely pointed out that this phase is likely to be overlooked because its detection is extremely difficult.

We previously[29] examined absorption of near ultraviolet photons in noncrystalline TiO_2 films. A nonresonant Raman spectroscopy study[31] showed that these films were vitreous (as distinguished from amorphous, in keeping with the aforementioned definition) and had SRO characteristic of crystalline anatase. The fundamental optical absorption edge was effectively modeled within the framework of the coherent potential approximation with Gaussian site disorder introduced into the valence and conduction bands of a perfect virtual anatase crystal. The films were then annealed to produce various amounts of crystalline anatase, hence LRO. The results reaffirmed a general rule by Tauc:[32] interband optical transitions described by wave functions localized over distances on the order of a lattice constant are relatively unchanged by disorder. The transfer of electronic charge *within* TiO_6 octahedral units (i.e., between nearest-neighbor Ti and O atoms) was found to be the key factor in determining the material's response to ultraviolet radiation, irrespective of the degree of LRO.

However, a solid's response to infrared photons is governed by the relative motion of atoms, and indeed may be different for crystalline and vitreous TiO_2.[33] The goals of the present paper are, therefore: (a) to determine the infrared reflection–absorption behavior of vitreous TiO_2 with anatase SRO, (b) to model this behavior by choosing an appropriate dielectric function, and (c) to identify the type of structural disorder that is commensurate with the experimental and theoretical modeling results.

Infrared reflection–absorption spectroscopy (IRAS) of solids was historically[33] used to measure vibrational modes. In a crystal, long wavelength vibrational modes are associated with atomic motion perpendicular and parallel to the direction of wave propagation. The two types of modes are denoted transverse optic (TO) and longitudinal optic (LO). For thin crystalline films (thickness$\ll$infrared wavelength), TO modes are detected as absorption bands in transmission and reflection spectra in both *s* and *p* polarization, whereas LO modes are detected only in *p* polarization.[34] Polarization-dependent bands are also detected in thin noncrystalline films, and have been attributed to TO-like or LO-like modes.[35–41]

In reality, however, the vibrational modes in a noncrystalline solid do not cleanly separate into atomic motion perpendicular and parallel to the propagation direction. Rather, the atomic displacements generally form a complicated pattern varying markedly in magnitude and direction throughout the medium. Nonetheless, a noncrystalline solid can be described by a dielectric function, $\epsilon(\nu)$, that contains all the relevant microscopic information as far as the response to the incident electromagnetic wave is concerned. Such information includes the resonant frequencies of the individual vibrating units, their associated lifetimes, and their oscillator strengths (or effective charges). The dielectric function is also affected by coupling between units through the long-range Coulomb interaction as well as through short-range chemical bonding.

Thus, by modeling the dielectric function and comparing the results of theoretical IRAS spectra with experimental IRAS spectra, one can, in principle, deduce the value of the microscopic parameters of a noncrystalline solid. Furthermore, structural information concerning the shape, orientation, and distribution of the individual vibrating units can also be obtained.[42] Alternatively, if one is interested only in the electromagnetic response of macroscopic samples, one could forgo the microscopic information entirely and use the experimental IRAS spectra to deduce $\epsilon(\nu)$. Once $\epsilon(\nu)$ is determined, the electromagnetic response of any macroscopic sample of the noncrystalline solid can be found.

We report the optical response of sputter-deposited vitreous TiO_2 films with anatase SRO. Experimental IRAS spectra were obtained in the 100–1000 cm^{-1} wave number range. Our data were found to differ from those for single crystal anatase.[43] We therefore constructed a dielectric function to account for random orientational disorder within the films. Calculated energy loss functions and theoretical reflection–absorption spectra using this dielectric function were compared with experimental results. Good qualitative agreement between experimental and theoretical IRAS spectra indicates that orientational disorder is the important factor governing the reflection–absorption behavior of our vitreous films.

II. EXPERIMENTAL PROCEDURE

Titanium dioxide films (0.25-μm-thick film A and 0.70-μm-thick-film B), were grown by sputter deposition from a 99.995% Ti target in a radio-frequency-excited O_2 plasma as described in Ref. 29. Films were grown on substrates cut from a 99.0% pure rolled Al sheet.

Double-angle x-ray diffraction (XRD) was used to identify the small amount of nanocrystalline material in each film. Diffraction patterns were obtained using unresolved 0.15418-nm-wavelength Cu Kα radiation. Peak position ($2\theta_{hkl}$), maximum intensity (I_{max}), and full width at one-half maximum intensity (FWHM) were measured from high resolution scans of individual peaks. Phase identification, preferred orientation, and phase composition were determined

TABLE I. XRD parameters and crystallite size in titanium dioxide films on aluminum.

Film/Peak	I_{max} (cps)	FWHM (deg)	D (nm)
A/r (110)	60	0.65	24
A/a (101)	107	0.65	24
B/r (110)	287	0.50	17
B/a (101)	135	0.50	17

from these data. The Debye–Scherrer relationship[44] was used to estimate the crystallite dimension parallel to the growth direction, assuming the absence of peak broadening due to random lattice strain.

Infrared reflection–absorption spectroscopy data in the far-infrared spectra range were obtained with a Fourier transform infrared spectrometer by Bruker (Model IFS 113v) equipped with a polyethylene-supported polarizer. For each spectrum, 100 scans were taken at 4 cm^{-1} resolution and at an angle of incidence $\phi=45°$. (An oblique incident beam was required to observe LO-like features.) Measurements were made at a pressure of 1×10^{-3} Torr and room temperature. Middle-IRAS data was obtained with a Bruker V22 Fourier transform infrared spectrometer equipped with a ZnSe-supported polarizer. For each spectrum, 300 scans were taken at a resolution of 4 cm^{-1} and at an angle of incidence $\phi=45°$. Data were taken at ambient conditions. A bare Al substrate was used as reference for both far- and mid-IRAS measurements. Theoretical IRAS spectra were calculated from the Fresnel equations[34,45] using MATHEMATICA.

III. FILM STRUCTURE

The XRD spectra (not shown) of 0.25-μm-thick film A and 0.70-μm-thick film B had the following common features: (a) Reflections from both rutile and anatase phases were present. (b) The dominant anatase reflection was from (101) planes at $2\theta=25.4°$, with additional minor reflections from (004) planes at $2\theta\approx38°$ and (200) planes at $2\theta\approx48°$.[46] A comparison of peak intensities with that for a randomly oriented powder sample[46] showed that anatase preferably crystallized with (101) planes parallel to the substrate. (c) Solely rutile-(110) reflections were present, at $2\theta=27.5°$,[47] i.e., rutile crystallized with (110) planes parallel to the substrate. (d) All peaks were broad, suggesting nanocrystallinity. (e) All peaks had low intensity, indicating that a TiO_2 structure not detectable by XRD coexists along with the nanocrystalline phases.

The maximum intensity and FWHM for anatase-(101) and rutile-(110) peaks are recorded in Table I. For reference, the maximum intensities in Table I should be compared to a fully crystallized, single (110) orientation, 0.25-μm-thick rutile film with a first order diffraction peak intensity of 2300 cps and a FWHM equal to that for instrumental broadening effects. The average minimum crystallite dimension (D) parallel to the growth direction anatase-(101) and rutile-(110) are included in Table I.

The detectable rutile volume fraction in each film was determined using the external standard method.[44] The formalism developed for the application of this method to disordered TiO_2 films is given in Ref. 29. In summary, the volume fraction of the rutile component of a uniform multiphase mixture, f_r, is related to the integrated intensity of a specific rutile reflection, $I_{hkl}^{(r)}$, as

$$\frac{I_{hkl}^{(r)}}{I_{hkl}^{(s)}}=\frac{f_r}{f_s}, \tag{1}$$

where $I_{hkl}^{(s)}$ is the XRD intensity of a rutile standard that has the same preferred orientation as the film to be analyzed, and f_s (standard) is the volume fraction of rutile in the standard and is equal to unity by definition. In order to apply Eq. (1) to our films, we used a previously fabricated, fully crystallized rutile standard film:[29] an annealed 0.25-μm-thick TiO_2 film on fused silica whose XRD pattern showed two orders of a single rutile-(110) peak. For film A, Eq. (1) becomes: $f_r(\text{film A})=I_{r110}(\text{film A})/I_{r110}(\text{standard})$. A similar procedure was followed to calculate the rutile volume fraction in film B, with the added stipulation that the thickness difference between film B and film A must be taken into account. A previous calculation[29] lead to the relationship: $f_r(\text{film B})=0.43[I_{r110}(\text{film B})/I_{r110}(\text{standard})]$. The volume fraction of rutile in each film is recorded in Table II.

TABLE II. Phase composition of titanium dioxide films on aluminum.

Film	$f_r(\times10^2)$	$f_a(\times10^2)$	$f_a(\times10^2)$
A	3.7	3.2	93.1
B	2.0	6.5	91.5

Since both films contain a large component that cannot be detected by XRD, a straightforward calculation using $f_a=1-f_r$, where f_a is the anatase volume fraction, is not valid. Furthermore, precise calculation of f_a using the external standard method, analogous to the above calculation for f_r, requires a completely crystallized anatase external standard with the same preferred orientation as the films. Preparation of an anatase film standard is not possible by annealing because the transformation of crystalline anatase to rutile occurs in these films before complete crystallization of the noncrystalline component.[21,22] However, the standardless direct comparison method of Averbach and Cohen[48,49] will yield a reasonable estimate of f_a. In this case, the anatase-(101) peak is compared to the rutile-(110) peak in both films: $I_{a(101)}/I_{r(110)}\approx X_a f_a/X_r f_r$. X for each component is the product of five factors: (a) the inverse of the square of the unit cell volume, (b) the square of the absolute value of the structure factor, (c) the multiplicity of a particular set of diffracting planes, (d) the Lorentz polarization factor, and (e) the Debye–Waller temperature factor. Calculation[44] of these factors leads to the relationship $I_{a(101)}/I_{r(110)}\approx0.65f_a/f_r$. Substitution of the relative anatase-(101) and rutile-(110) integrated intensities into the above expression yields an estimate of the volume fraction of detectable nanocrystalline anatase, recorded in Table II, neglecting the small contribution of nanocrystalline anatase with other than a (101) orien-

tation. Also recorded is the total volume fraction of material that cannot be detected by XRD, calculated from $f_\alpha = 1 - (f_a + f_r)$.

Nonresonant Raman spectra (see Ref. 31) of films on Si grown under the same conditions as films A and B showed four absorption peaks attributable to Raman-active vibrational modes of anatase.[50] The assignment and wave numbers of these vibrations are: (1) unresolved B_{1g} at 144 cm^{-1} and E_g at 147 cm^{-1}, (2) B_{1g} and A_{1g} at 198 cm^{-1}, (3) B_{1g} at 398 cm^{-1}, and (4) E_g at 640 cm^{-1}. These peaks account for five of the six Raman-active vibrational modes of anatase. A sixth mode, E_g at 515 cm^{-1}, was masked in the films by the strong LO phonon mode of the Si substrate at 520 cm^{-1}. Markedly, the three characteristic rutile modes, E_g at 448 cm^{-1}, A_{1g} at 612 cm^{-1}, and B_{1g} at 827 cm^{-1}, were absent from spectra of films A and B.

The XRD data given in Table II show that two nanocrystalline phases, anatase and rutile, are present in both films A and B, but these phases account for a small amount of the films' volume. Of the detectable nanocrystalline material, less than 4% in film A and 2% in film B is crystalline rutile. Raman spectroscopy of companion films on Si detects only anatase Ti–O short-range order. From these results, we conclude that greater than 96% of film A and 98% of film B is comprised of material that has anatase short-range order.

IV. EXPERIMENTAL IRAS SPECTRA

The experimental IRAS spectra for films A and B are shown in Figs. 1 and 2, respectively. In these figures, the quantity $R_{\text{film+Al}}/R_{\text{Al}}$ is graphed as a function of wave number, ν/c, from 10^2 to 10^3 cm^{-1}, where $R_{\text{film+Al}}$ is the reflectivity of the sample obtained using *p* or *s* polarization, and R_{Al} is the reflectivity of the bare Al substrate. The insert shows an expanded region from 225–475 cm^{-1} to highlight small features in that spectral range. [For the sake of comparison, theoretical spectra are included in Figs. 1 and 2 (broken curves), but discussion of these curves is postponed until Sec. V.] The spectral position of all features is recorded in Table III.

With respect to film A, Fig. 1 shows that absorption bands are present at 260, 355, and 442 cm^{-1} when an *s*-polarized beam is used. Absorption bands at 260, 443, and 853 cm^{-1} (with a shoulder at 962 cm^{-1}) occur for *p* polarization. In addition, weak features occur in R_p between 300–400 cm^{-1}.

With respect to film B, Fig. 2 shows absorption bands at 259 and 439 cm^{-1} when an *s*-polarized beam is used. In addition, extremely weak features centered at ~310 and ~345 cm^{-1} are present in R_s. Absorption bands at 258, 438, and 849 cm^{-1} (with shoulders at 785 and 962 cm^{-1}) are observed for *p* polarization. In addition, the features at ~310 and ~345 cm^{-1} in R_s broaden into a single, extremely weak, featureless band extending from 300–350 cm^{-1} in R_p.

Comparing the spectra of films A and B, three absorption bands can be identified as having the same frequency within experimental error. Two absorption bands common to both polarizations of both films have average frequencies of 259 cm^{-1} and 441 cm^{-1}. Furthermore, a band with an average

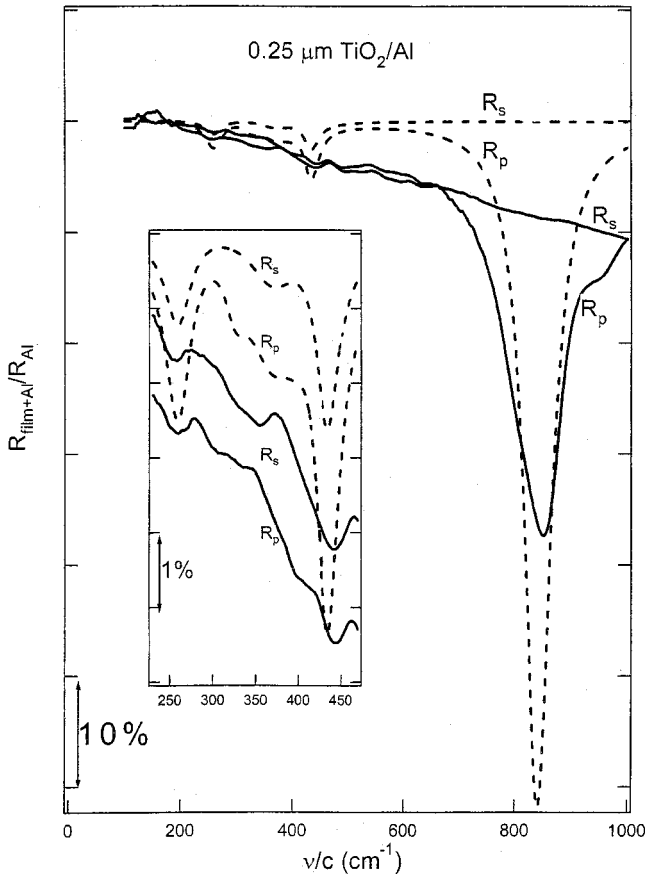

FIG. 1. Solid curves show experimental IRAS spectra and broken curves show theoretical IRAS spectra for 0.25-μm-thick film A. $R_{\text{film+Al}}/R_{\text{Al}}$ is graphed as a function of wave number, ν/c. The insert shows an expanded region from 225–475 cm^{-1} to highlight small features in that spectral range.

frequency of 851 cm^{-1} occurs in the *p*-polarization spectra of both films and is absent from their *s*-polarization spectra.

The above results should be compared to those of Trasferetti *et al.*,[51] who used IRAS over a spectral range of 400–1400 cm^{-1} to study plasma-enhanced chemical vapor deposited noncrystalline TiO_2 on Al. The SRO was not measured by an independent method and was unspecified. Only one peak was reported, a single broad band that appeared in R_p, but not in R_s, centered at ~850 cm^{-1} for an incident beam angle of 50°. This frequency is in excellent agreement with the highest frequency absorption band in our films. Trasferetti *et al.* discussed this band's frequency as being in disagreement with the prominent LO mode of rutile at 806 cm^{-1},[52] but we suggest, on the basis of agreement with our spectra, that the SRO order of their films was most likely anatase.

V. THEORETICAL IRAS SPECTRA

Gonzalez *et al.*[43] recently published experimentally determined TO and LO phonon frequencies of single-crystal anatase in which the applied electric field, **E**, was either parallel or perpendicular to the **c** crystallographic vector. Those researchers found that **E**∥**c** gave rise to one pair of A_{2u} modes: a transverse optical phonon mode at 367 cm^{-1} and a longitudinal optical phonon mode at 755 cm^{-1} and **E**⊥**c** gave

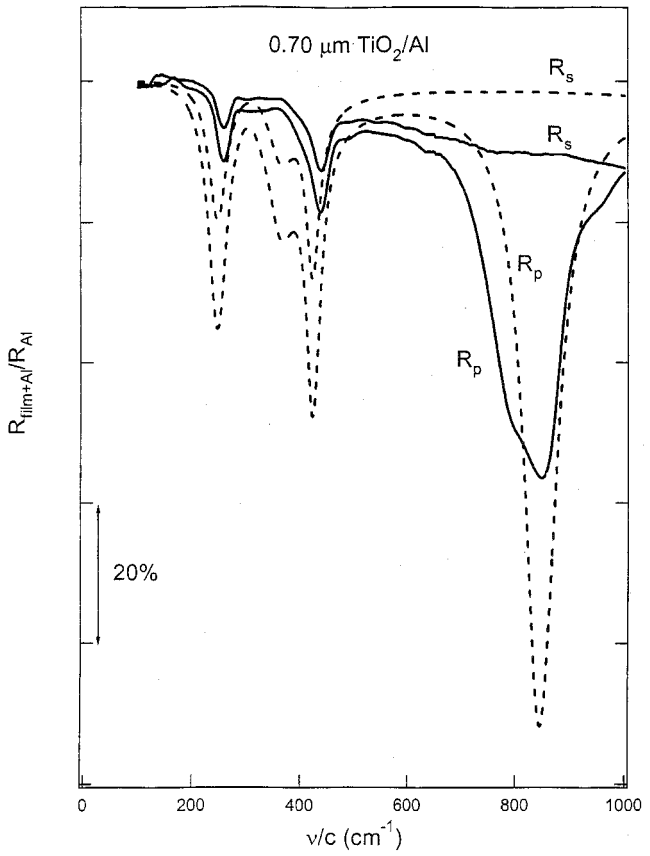

FIG. 2. Solid curves show experimental IRAS spectra and broken curves show theoretical IRAS spectra obtained using *s* and *p* polarization for 0.70-μm-thick film B. $R_{\text{film+Al}}/R_{\text{Al}}$ is graphed as a function of wave number, ν/c.

rise to two pairs of E_u modes: a low frequency pair at 262 cm^{-1} (TO)–366 cm^{-1} (LO) and a high frequency pair at 435 cm^{-1} (TO)–876 cm^{-1} (LO). However, a comparison of single-crystal data with the experimental IRAS data (Table III) shows that only the two E_u (TO) modes correlate with bands in both films A and B.

We suggest that the primary cause of the disparity between our experimental results and those for single-crystal anatase is that the Ti–O units in the vitreous film are not solely in either the $\mathbf{E}\perp\mathbf{c}$ or $\mathbf{E}\|\mathbf{c}$ orientation. Consequently, the electromagnetic response of the film is described not by either of the dielectric functions $\epsilon_\perp(\nu)$ or $\epsilon_\|(\nu)$ alone. In the following text, we construct a suitable dielectric function, $\epsilon(\nu)$, that is the directional average of $\epsilon_\perp(\nu)$ and $\epsilon_\|(\nu)$. We then show that the theoretical spectra calculated using $\epsilon(\nu)$ do, in fact, differ from the reported spectra for single-crystal anatase.

In order to calculate theoretical IRAS spectra, we must determine the reflection coefficient for infrared radiation incident from air onto a dielectric film that lies on a metal substrate, i.e., the standard electromagnetic-wave-reflection problem for a ''three-layer model.'' Its explicit solution, embodied in the Fresnel equations, can be found, for example, in the work of Berreman[34] and Hansen.[45] The dielectric function of the film and the metal, denoted $\epsilon(\nu)$ and $\epsilon_m(\nu)$, respectively, are required to apply this solution. [The corresponding indices of refraction are $\epsilon(\nu)^{1/2}$ and $\epsilon_m(\nu)^{1/2}$.]

TABLE III. Wave number of absorption bands of titanium dioxide films on aluminum.

Film	Polarization	ν/c (cm^{-1})	
		Experimental	Theoretical
A	*s*	260	259
		355	374
		442	434
A	*p*	260	261
		a	b
		443	435
		853, c	841
B	*s*	259	247
		d	367
		439	423
B	*p*	258	247
		e	368
		438	423
		849, (c,f)	846

[a]Weak features between 300–400 cm^{-1}.
[b]Weak bands at 330 and 380 cm^{-1}.
[c]Shoulder at 962 cm^{-1}.
[d]Extremely weak bands at ~310 and ~345 cm^{-1}.
[e]Broad, extremely weak band from 300–350 cm^{-1}.
[f]Shoulder at 785 cm^{-1}.

In constructing our model, we assume that each individual Ti–O unit, which may be as small as a single TiO_6 molecule, in the vitreous structure has the same polarizability and the same dielectric function that the unit would have in an anatase crystal environment. We are thus considering orientational disorder of Ti–O units, but ignoring chemical effects, local strains, and local defects that might cause the polarizability parameters of an individual Ti–O unit to be different in the vitreous solid compared to a perfect crystal. (Such parameters include the frequencies, oscillator strengths, and lifetimes of the local vibrational modes.) Evidence that this type of orientational disorder is the dominant contribution to line broadening in the spectra of noncrystalline films has been given by Ovchinnikov and Wight in their studies of N_2O, CO_2, and O_3 films.[42]

In keeping with the assumption of randomly oriented Ti–O units described by the dielectric functions appropriate to the crystal, we construct a dielectric function that is the directional average of the dielectric functions for a crystal in the $\mathbf{E}\perp\mathbf{c}$ and $\mathbf{E}\|\mathbf{c}$ orientations:

$$\epsilon(\nu)=[2\epsilon_\perp(\nu)+\epsilon_\|(\nu)]/3, \tag{4}$$

where $\epsilon_\perp(\nu)$ and $\epsilon_\|(\nu)$ are obtained from the factorized form of the dielectric function for the $\mathbf{E}\perp\mathbf{c}$ and $\mathbf{E}\|\mathbf{c}$ orientations, respectively, using the resonant frequencies and damping factors for phonon modes given in Ref. 43. The same prescription for constructing an effective dielectric function was used by Aoki *et al.* to model polycrystalline MgF_2 IRAS spectra.[53] The real and imaginary parts of the dielectric functions $\epsilon_\|(\nu)$, $\epsilon_\perp(\nu)$, and $\epsilon(\nu)$ are shown in Fig. 3.

For a single crystal, the TO loss function, defined as the imaginary part of the dielectric function, has a peak at a TO mode resonance. These resonances can be seen in the graphs of $\text{Im}[\epsilon_\|(\nu)]$ [Fig. 3(a)] and $\text{Im}[\epsilon_\perp(\nu)]$ [Fig. 3(b)] for single-crystal anatase. Consistent with established nomenclature, we refer to $\text{Im}[\epsilon(\nu)]$ as the TO loss function for the vitreous

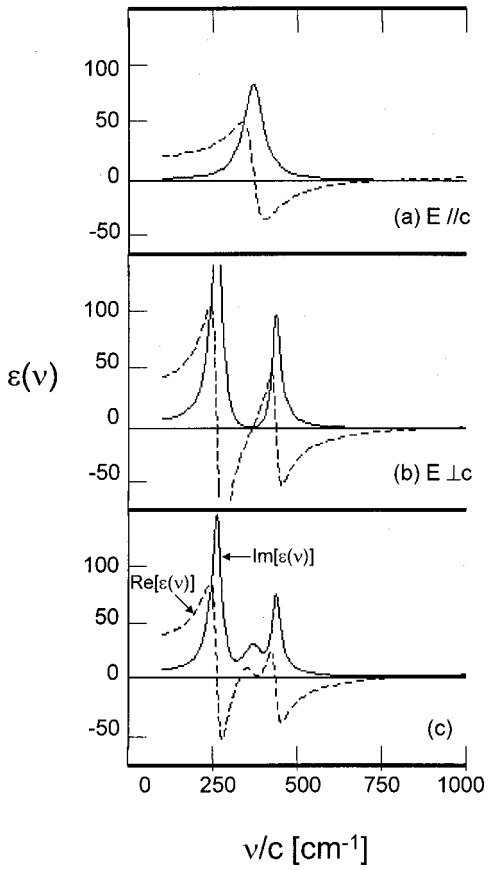

FIG. 3. The real (broken curve) and imaginary (solid curve) parts of the dielectric function vs wave number, showing (a) $\epsilon_{\|}(\nu)$, (b) $\epsilon_{\perp}(\nu)$, and (c) $\epsilon(\nu)=[2\epsilon_{\perp}(\nu)+\epsilon_{\|}(\nu)]/3$.

films. The peaks in $\mathrm{Im}[\epsilon(\nu)]$ resulting from Eq. (4) are recorded in Table IV. These peaks are essentially at the same frequencies as the TO loss function peaks of the anatase single crystal.

Likewise, for a single crystal, the LO loss function, defined as the imaginary part of the negative inverse dielectric function, has a peak at an LO mode resonance. These resonances can be seen in the graphs of $\mathrm{Im}[-1/\epsilon_{\|}(\nu)]$ [Fig. 4(a)] and $\mathrm{Im}[-1/\epsilon_{\perp}(\nu)]$ [Fig. 4(b)] for an anatase single crystal. Again, using established nomenclature, $\mathrm{Im}[-1/\epsilon(\nu)]$ is referred to as the LO loss function for the vitreous films. The peaks in $\mathrm{Im}[-1/\epsilon(\nu)]$ resulting from Eq. (4) are recorded in Table IV. Unlike the case of the TO loss function peaks, the LO loss function peaks are significantly different from those for single-crystal anatase. Notably, the strong high-frequency peak in $\mathrm{Im}[-1/\epsilon(\nu)]$ is at 840 cm^{-1} and lies between the

TABLE IV. Wave numbers of theoretical loss function peaks [see Figs. 3(c) and 4(c)].

Loss function peak	ν/c (cm^{-1})	Maximum intensity
TO: $\mathrm{Im}[\epsilon(\nu)]$	262	158
	369	32.6
	436	80.3
LO: $\mathrm{Im}[-1/\epsilon(\nu)]$	328	0.06
	396	0.04
	840	2.62

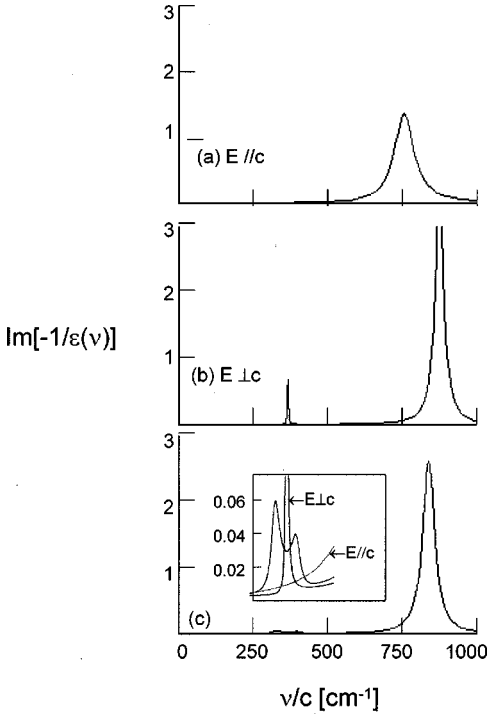

FIG. 4. LO loss function vs wave number showing (a) $\mathrm{Im}[-1/\epsilon_{\|}(\nu)]$, (b) $\mathrm{Im}[-1/\epsilon_{\perp}(\nu)]$, and (c) $\mathrm{Im}[-1/\epsilon(\nu)]$.

anatase single crystal LO loss peaks at 755 cm^{-1} [Fig. 4(a)] and 876 cm^{-1} (Fig. 4b) for $\mathbf{E}\|\mathbf{c}$ and $\mathbf{E}\perp\mathbf{c}$ beam configurations, respectively.

The final ingredient needed to calculate theoretical IRAS spectra is the dielectric function of the metal. Here we assume the free-electron model, and take (in Gaussian units)

$$\epsilon_m(\nu)=1+2i\sigma(\nu)/\nu, \tag{5}$$

where $\sigma(\nu)$ is the frequency-dependent conductivity, which has the Drude form,

$$\sigma(\nu)=\sigma(0)/(1-2\pi i\nu\tau), \tag{6}$$

where τ is the relaxation time. In our calculations, we used the values $\sigma(0)=3.67\times10^{17}\,\mathrm{s}^{-1}$ and $\tau=0.80\times10^{-14}\,\mathrm{s}$ for Al at room temperature.[54]

The theoretical reflection coefficients for films A and B are shown for *s* polarization (R_s) in Figs. 5 and 6, and for *p* polarization (R_p) in Figs. 7 and 8. Each figure is comprised of three panels calculated using a dielectric function: (a) $\epsilon_{\|}(\nu)$, (b) $\epsilon_{\perp}(\nu)$, and (c) $\epsilon(\nu)$. The wave numbers at the peaks of the absorption bands (reflectivity minima for case (c)) are recorded in Table III.

With respect to film A, Fig. 5(c) shows that absorption bands are present at 259, 374, and 434 cm^{-1} when an *s*-polarized beam is used. Figure 6(c) shows absorption bands at 261, 435, and 841 cm^{-1} occur for *p* polarization. In addition, weak bands occur in R_p at 330 and 380 cm^{-1}.

With respect to film B, Fig. 7(c) shows absorption bands at 247, 367, and 423 cm^{-1} when an *s*-polarized beam is used. Figure 8(c) shows absorption bands at 247, 368, 423, and 846 cm^{-1} for *p* polarization.

A comparison of Figs. 5(c) and 7(c) (film A) with Figs. 6(c) and 8(c) (film B) shows that for the same polarization

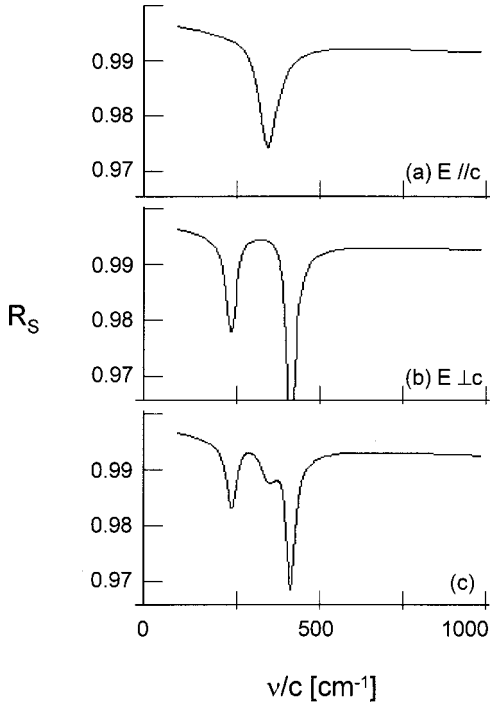

FIG. 5. Theoretical reflection coefficients for film A on aluminum for *s*-polarized beam conditions as a function of wave number using (a) $\epsilon_{\parallel}(\nu)$, (b) $\epsilon_{\perp}(\nu)$, and (c) $\epsilon(\nu)=[2\epsilon_{\perp}(\nu)+\epsilon_{\parallel}(\nu)]/3$.

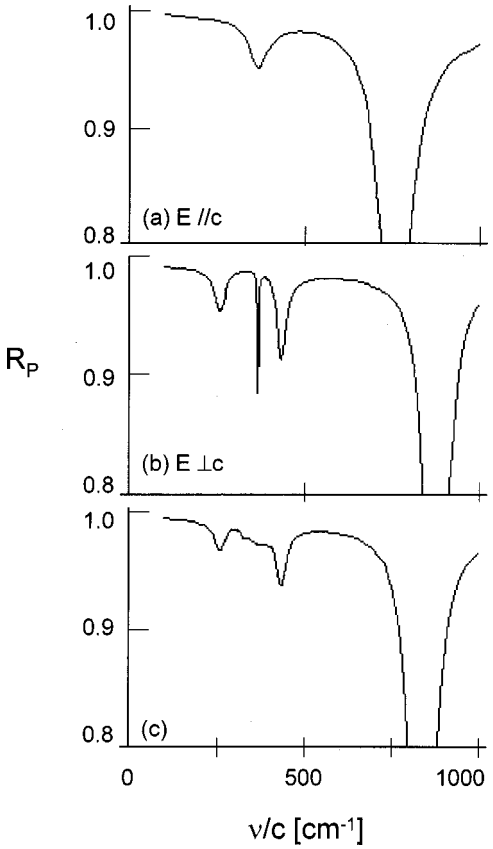

FIG. 7. Theoretical reflection coefficients for film A on aluminum for *p*-polarized beam conditions as a function of wave number using (a) $\epsilon_{\parallel}(\nu)$, (b) $\epsilon_{\perp}(\nu)$, and (c) $\epsilon(\nu)=[2\epsilon_{\perp}(\nu)+\epsilon_{\parallel}(\nu)]/3$.

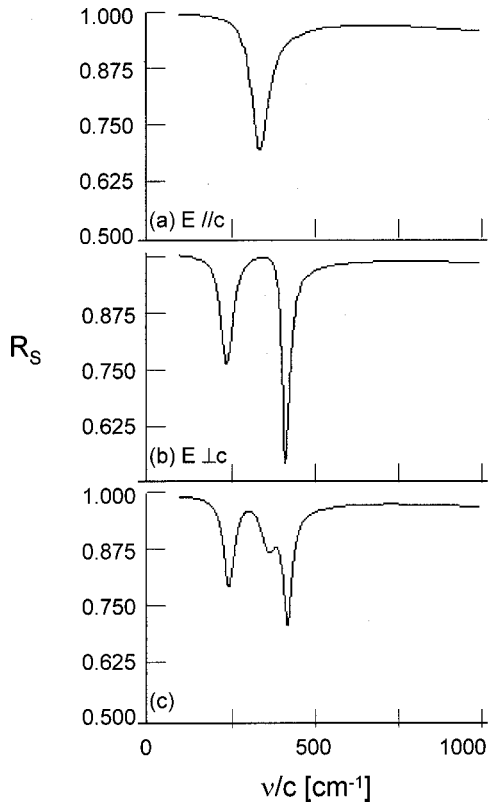

FIG. 6. Theoretical reflection coefficients for film B on aluminum for *s*-polarized beam conditions as a function of wave number using (a) $\epsilon_{\parallel}(\nu)$, (b) $\epsilon_{\perp}(\nu)$, and (c) $\epsilon(\nu)=[2\epsilon_{\perp}(\nu)+\epsilon_{\parallel}(\nu)]/3$.

state, the shapes of the theoretical spectra are similar, but there are significant changes in peak intensity, as might be expected in going from a thinner to thicker film, and small shifts in peak position.

VI. DISCUSSION

A. Comparison of experimental and theoretical IRAS spectra

The quantity $R_{\text{film+Al}}/R_{\text{Al}}$, calculated using $\epsilon(\nu)$, is included in Figs. 1 and 2 (broken curves), along with the experimental curves. A comparison of the experimental and theoretical spectra for both films shows similar peak position, but the theoretical bands are more intense. In addition, a band at 367–368 cm^{-1} in the theoretical spectra of film B is absent from the corresponding experimental spectra.

The experimental and theoretical absorption band frequencies for film A (Table III) can be compared with TO and LO loss function peaks (Table IV). Both the experimental and theoretical band frequencies correlate well with TO loss function peaks at 262 and 435 cm^{-1}. Weaker bands in experimental R_s at 355 cm^{-1} and in theoretical R_s at 374 cm^{-1} can be associated with an TO loss function peak at 367 cm^{-1}. A strong band in experimental R_p at 853 cm^{-1} and theoretical R_p at 841 cm^{-1} can be associated with an LO loss function peak at 840 cm^{-1}. Note that this band is absent in R_s. We therefore associate this band with an LO-like reso-

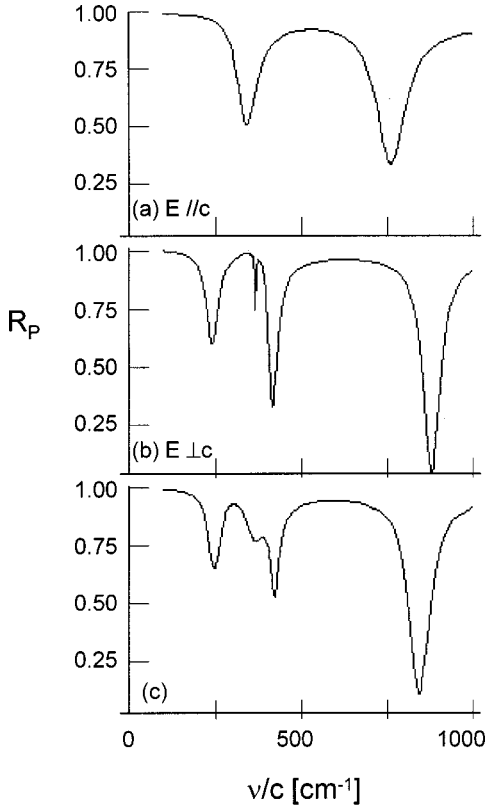

FIG. 8. Theoretical reflection coefficients for film B on aluminum for *s*-polarized beam conditions as a function of wave number using (a) $\epsilon_{\parallel}(\nu)$, (b) $\epsilon_{\perp}(\nu)$, and (c) $\epsilon(\nu)=[2\epsilon_{\perp}(\nu)+\epsilon_{\parallel}(\nu)]/3$.

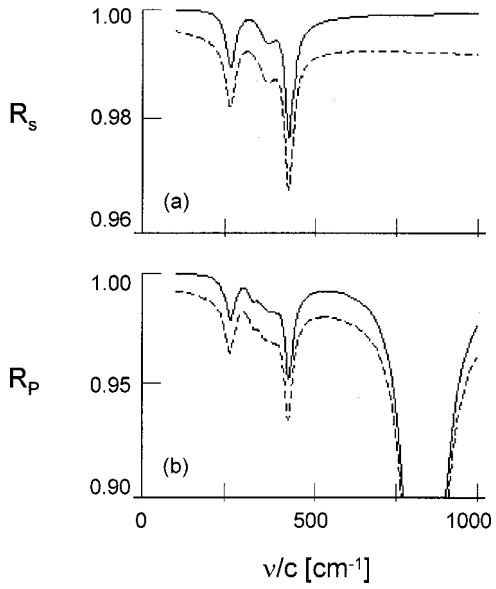

FIG. 9. Theoretical reflection coefficients (a) R_s and (b) R_p as a function of wave number for film A on perfect (solid curve) and real metal (broken curve) substrates.

nance in film A, a manifestation of the Berreman effect,[34] which finds LO resonances in *p*-polarized spectra, but not in *s*-polarized spectra. Similarly, weak structures in the R_p spectrum can be traced to minor peaks of the LO loss function at 328 and 396 cm^{-1}.

The experimental and theoretical absorption band frequencies for film B (Table III) can be compared with TO and LO loss function peaks (Table IV). Both the experimental and theoretical band frequencies can be correlated with TO loss function peaks at 262 and 435 cm^{-1}. A strong band in experimental R_p at 849 cm^{-1} and in theoretical R_p at 846 cm^{-1} is in good agreement with an LO loss function peak at 840 cm^{-1}. As in the case of film A, these peaks are absent from R_s, again, the Berreman effect.

The experimental splitting, $\Delta_{\mathrm{LO-TO}}$, of the high frequency ''LO–TO'' pair for both films is equal to 410–411 cm^{-1}, in excellent agreement with that predicted from the difference in corresponding theoretical LO–TO loss function peaks in the vitreous films, $\Delta_{\mathrm{LO-TO}}=404\,cm^{-1}$. For a crystalline solid, this correspondence yields the width of the high reflectivity Reststrahlen band, and $\Delta_{\mathrm{LO-TO}}=441\,cm^{-1}$, for the analogous high frequency $\mathbf{E}\perp\mathbf{c}$ LO–TO mode pair in single-crystal anatase.[43] These results show that introducing random disorder into an anatase crystal has the effect of narrowing the Reststrahlen region. Furthermore, $\Delta_{\mathrm{LO-TO}}$ in a crystalline solid is related to its ionicity,[33] and this concept has been extended to glasses as well.[40] The fact that $\Delta_{\mathrm{LO-TO}}$ in the vitreous films is reduced from the single crystal value indicates that random orientational disorder reduces the effective dipole moment per unit film volume.

There is also a difference to note in the experimental versus theoretical spectra when comparing the frequency of equivalent bands between films. Referring to Table III, the difference in experimental frequencies of equivalent bands is within experimental error when comparing films A and B. However, this is not in general the case for the theoretical band frequencies. For example, experimental R_p bands at 260, 443, and 853 cm^{-1} in film A shift by -2, -5, and -4 cm^{-1}, respectively, in film B (within experimental error), whereas the theoretical shifts in these bands in going from film A to B are -14, -12, and $+5$ cm^{-1}, respectively.

B. Connection between absorption bands and loss functions

To understand the relationship of the theoretical absorption bands to the loss functions for the vitreous films, $\mathrm{Im}[\epsilon(\nu)]$ and $\mathrm{Im}[-1/\epsilon(\nu)]$, and in particular to trace the source of the shifts in the theoretical spectra with increasing film thickness, we next consider the case in which the substrate is a perfect metal $[\sigma(0)\rightarrow\infty]$. Figure 9 compares R_s and R_p curves for film A on perfect and real metal substrates and shows the validity of the $\sigma(0)\rightarrow\infty$ assumption. The effect of finite conductivity is to increase the overall absorption (or decrease the reflectivity), but there is very little change in the shape of the curves or in the positions of the absorption bands. The same conclusion applies to film B, where the perfect-metal and real-metal results are actually much closer together than they are for film A.

The expressions for R_s and R_p for a film of thickness d on a perfect metal substrate can be obtained from the Berreman[34] or Hansen[45] expressions by taking the limit $\sigma(0)\rightarrow\infty$ (also see Ref. 55). The results for both polarizations can be written in the following compact form,

$$R=|(1+i\alpha\tan\beta d)/(1-i\alpha\tan\beta d)|^2, \tag{7}$$

where $\alpha=(\cos\phi)[\epsilon(\nu)-\sin^2\phi]^{-1/2}$ for *s* polarization, $\alpha=[\epsilon(\nu)-\sin^2\phi]^{1/2}/[\epsilon(\nu)\cos\phi]$ for *p* polarization, and $\beta=k_0[\epsilon(\nu)-\sin^2\phi]^{1/2}$ with $k_0=2\pi\nu/c$.

Expanding Eq. (7) for a very thin film, i.e., for $|\beta d|\ll 1$ and $k_0 d\ll 1$, we find,

$$R_s=1-(4/3)(\cos\phi)(k_0 d)^3\,\mathrm{Im}[\epsilon(\nu)], \tag{8}$$

and

$$R_p=1-(4/3)(1/\cos\phi)(k_0 d)^3\,\mathrm{Im}[\epsilon(\nu)] + 4(\sin^2\phi/\cos\phi)(k_0 d)\mathrm{Im}[1/\epsilon(\nu)], \tag{9}$$

where higher-order terms in $k_0 d$ in both $\mathrm{Im}[\epsilon(\nu)]$ and $\mathrm{Im}[1/\epsilon(\nu)]$ have been omitted, and ϕ is assumed to be not too close to 90°. The condition $|\beta d|\ll 1$ can be relaxed to $|\beta d|<0.5$ since this condition is only used to justify the series expansion $\tan\beta d=\beta d+(\beta d)^3/3$ in Eq. (7). We have numerically verified that Eqs. (8) and (9) are good approximations to the ''exact'' theoretical results, from Eq. (7), for film A on an ideal-metal substrate, except that Eq. (9) overestimates the strength of the absorption band at 840 cm^{-1} in the R_p spectrum.

Equations (8) and (9) show that for very thin films, the absorption bands for *s* polarization are located at the peaks of $\mathrm{Im}[\epsilon(\nu)]$, and for *p* polarization the absorption bands are located at the peaks of $\mathrm{Im}[\epsilon(\nu)]$ and $\mathrm{Im}[-1/\epsilon(\nu)]$. This phenomenon is the essence of the Berreman effect: absorption bands for thin films occur in *p* polarization, but not in *s* polarization at the peaks of $\mathrm{Im}[-1/\epsilon(\nu)]$, which is the LO loss function for our film. Further, note that for very thin films, the *p*-polarization absorption is dominated by $\mathrm{Im}[-1/\epsilon(\nu)]$ peaks rather than by $\mathrm{Im}[\epsilon(\nu)]$ peaks because absorption bands associated with $\mathrm{Im}[\epsilon(\nu)]$ peaks are of order $(k_0 d)^3$, while the absorption bands associated with $\mathrm{Im}[-1/\epsilon(\nu)]$ peaks are of order $k_0 d$.

To understand the physical origin of these absorption band intensities for very thin films, note that the electric field, **E** in the film is parallel to the film surface in *s*-polarization, whereas in *p* polarization **E** is dominated by a component $\mathbf{E}_\perp$ that is perpendicular to the surface. The absorption due to the parallel component of **E** is proportional to the TO loss function $\mathrm{Im}[\epsilon(\nu)]$, and the absorption due to $\mathbf{E}_\perp$ is proportional to the LO loss function $\mathrm{Im}[-1/\epsilon(\nu)]$. This is a very general statement about $\epsilon(\nu)$ and absorption bands in very thin films, regardless of the physical processes occurring in the film. Thus, despite our use of the usual terminology of TO and LO loss functions for $\mathrm{Im}[\epsilon(\nu)]$ and $\mathrm{Im}[-1/\epsilon(\nu)]$, respectively, this does not imply that vibrational modes with atomic motion perpendicular or parallel to the direction of propagation exist in our films. Indeed, Eqs. (8) and (9) would hold in the hypothetical case that a film did not support any vibrational modes at all, provided of course that all relevant dynamical processes were included in $\epsilon(\nu)$.

The relative strength of *s*-polarization and *p*-polarization absorption bands can be understood from the fact that the electric field **E** in the film is much weaker for an *s*-polarized beam than for a *p*-polarized beam.[56] This is a consequence of the boundary condition requiring the tangential component of **E** to be continuous across the film/metal interface. Since **E** vanishes in a perfect metal, and **E** is parallel to the surface only for the *s*-polarized beam, there must be a node in **E** at the film/metal interface for an *s*-polarized beam, but not for a *p*-polarized beam. More quantitatively, note that for *s* polarization, the sine-wave standing wave pattern for **E** in a very thin film results in an essentially linear variation for **E**, rising from zero at the film/metal interface to a constant at the air/film interface. Since the absorbed power is proportional to integral of $|\mathbf{E}|^2$ over the film volume, we deduce that the band intensity is proportional to $(k_0 d)^3$ for *s* polarization. For *p* polarization, on the other hand, **E** contains a dominant component $\mathbf{E}_\perp$, that is perpendicular to the film surface, and this component has no node at the film/metal boundary. The band intensity is now proportional to $k_0 d$, since $|\mathbf{E}|^2$ is essentially constant throughout the film and the *d* dependence of the absorbed power enters only through the volume integral.

For film A, the conditions $k_0 d\ll 1$ and $|\beta d|<0.5$ are both satisfied. Thus, film A is in the very-thin-film limit, so Eqs. (8) and (9) are applicable, and therefore absorption bands do occur at the peaks of $\mathrm{Im}[\epsilon(\nu)]$ and $\mathrm{Im}[-1/\epsilon(\nu)]$. For film B, however, $|\beta d|>1$ in the vicinity of the peaks in $\mathrm{Im}[\epsilon(\nu)]$. This difference accounts for the shifts in the theoretical absorption band frequencies associated with the peaks of $\mathrm{Im}[\epsilon(\nu)]$ in going from film A to film B. If film B was still in the very-thin-film limit, the absorption bands in the theoretical spectra for this film would remain where they are for film A, consistent with our experimental observation. The reason for the frequency shifts in the theoretical spectra appears to be that our $\epsilon(\nu)$ expression, determined from Eq. (4), is too resonant, i.e., the values of $\epsilon(\nu)$ at the TO loss function peaks are too large. A sharp resonance would also account for the theoretical absorption bands being more intense than the experimental absorption bands.

C. Choice of dielectric function

The problem of constructing an appropriate dielectric function for the vitreous films starting from orientationally disordered anatase Ti–O units is a difficult one. Within a mean-field-theory approach, this requires consideration of local effective fields in inhomogeneous media.[57] The result depends on the shape of the unit and its orientation with respect to the macroscopic electric field **E**. The choice of Eq. (4) for $\epsilon(\nu)$ implies that (on average) the effective field acting on a unit is the macroscopic electric field in the medium, or, in other words, there are no local-field corrections.[57,58] Strictly speaking, such a result is valid only if the individual units have rodlike, needlelike, or platelike shapes with the long axis along the direction of **E**.[57,58] If, on the other hand, the units are platelike and are oriented perpendicular to **E**, the correct choice would be given by the ''parallel capacitor formula,'' $\epsilon(\nu)^{-1}=[2\epsilon_\perp(\nu)^{-1}+\epsilon_\parallel(\nu)^{-1}]/3$.[58] Clearly, in the latter case, one would find strong absorption bands in *p*-polarized spectra at the LO mode resonances in both $\epsilon_\perp(\nu)$ and $\epsilon_\parallel(\nu)$. This is not the case in our experiments. Furthermore, dielectric functions based on a preferred geometrical

arrangement of units that are either parallel or perpendicular to **E** can be excluded because the direction of **E** is different in *s* and *p* polarizations.

We have also considered alternative prescriptions for constructing a dielectric function within a mean-field-theory framework. IRAS spectra were calculated using dielectric functions obtained from effective-medium theory,[59] and from Maxwell–Garnett and Clausius–Mossotti expressions.[60] None of these dielectric functions resulted in reflectivity curves that fit the experimental data as well as those obtained from our original choice of $\epsilon(\nu)$ given by Eq. (4).

Evidently, there are significant contributions to inhomogeneous broadening that are left out of our model, which is a mean-field model consisting of component parts, $\epsilon_{\parallel}(\nu)$ and $\epsilon_{\perp}(\nu)$ that are those for a perfect anatase crystal. Part of the difficulty may be in the mean-field aspect of the model. By using an average (or effective-medium) prescription to construct a dielectric function, we are not faithfully including short-range correlations between dipoles in neighboring Ti–O units except in some mean-field manner. Perhaps even more significantly, we have neglected additional life-time broadening and frequency-shift effects that are associated with chemical bonding between Ti–O units that may differ from the chemical bonding in the crystalline material. This includes local strain fields and local defects in the vitreous films that are not present in crystalline material.

We have been able to infer from these studies that orientationally disordered Ti–O units with a local structure characteristic of anatase play a dominant role in the dielectric response of our vitreous films. Further refinement of our model will include consideration of local (dis)order, traceable to short-range correlations in the coupling and/or chemical bonding between neighboring Ti–O units.

VII. SUMMARY

We reported the optical response of sputter-deposited vitreous TiO_2 films with anatase short-range order. Experimental IRAS spectra were obtained in the 100–1000 cm^{-1} wave number range. Our data were found to differ from those for single crystal anatase. We constructed a dielectric function to account for random orientational disorder within the films. Calculated energy loss functions and theoretical reflection–absorption spectra using this dielectric function were compared with experimental results. Good qualitative agreement between experimental and theoretical IRAS spectra indicates that orientational disorder is the important factor governing the reflection–absorption behavior of our vitreous films.

ACKNOWLEDGMENTS

We thank Dr. J. D. DeLoach, M. A. MacLaurin, and E. E. Hoppe for technical assistance, Dr. A. V. Sklyarov for useful discussions, and U. W.-Milwaukee Chancellor N. L. Zimpher for creating AceLab (Advanced Coatings Experimental Laboratory), through which G. S., R. S. S., and C. R. A. were partially supported. The following grants are also acknowledged: NSF-DMR-9806055 and NSF-CHE-9984931 (CJH); NSF-ECS 9984225, ACS-PRF 34396-G5, and a Wisconsin Space Grant Consortium Fellowship (VVY).

[1] T. Nakayama, K. Onisawa, M. Fuyama, and M. Hanasono, J. Electrochem. Soc. **139**, 1204 (1992).
[2] K. Jurek, M. Guglielni, G. Kuncova, O. Renner, F. Lukes, M. Navratil, E. Rousky, V. Vorlicek, and K. Kokesova, J. Mater. Sci. **27**, 2549 (1992).
[3] K. S. Yeung and Y. W. Lam, Thin Solid Films **109**, 169 (1983).
[4] B.-H. Jun *et al.*, Appl. Opt. **36**, 1482 (1997).
[5] E. Sirbegovic, M. Cevro, and I. Tucak, Vacuum **43**, 723 (1992).
[6] J. D. DeLoach and C. R. Aita, J. Mater. Sci. Lett. **19**, 1123 (2000).
[7] W. L. Bragg, *Atomic Structure of Minerals* (Cornell University Press, Ithaca, 1937), pp. 102–106.
[8] J. G. Clark, *The Chemistry of Titanium and Vanadium* (Elsevier, New York, 1968), pp. 66–277.
[9] F. Dachille, P. Y. Simons, and R. Roy, Am. Mineral. **53**, 1929 (1968).
[10] S.-D. Mo and W. Y. Ching, Phys. Rev. B **51**, 13023 (1995).
[11] K. Kosuge, *Chemistry of Non-stoichiometric Compounds* (Oxford University Press, Oxford, UK, 1994), pp. 121–128.
[12] F. P. Felner, *Low Temperature Oxidation* (Wiley-Interscience, New York, 1981), pp. 31–49 and references therein.
[13] M. Shiojiri, J. Phys. Soc. Jpn. **21**, 335 (1966).
[14] T. M. Salama, T. Tanaka, T. Yamaguchi, and K. Tanabe, Surf. Sci. Lett. **227**, L100 (1990).
[15] W. G. Lee, S. I. Woo, J. C. Kim, S. H. Choi, and K. H. Oh, Thin Solid Films **237**, 105 (1994).
[16] D. G. Howitt and A. B. Harker, J. Mater. Sci. **2**, 201 (1987).
[17] L. S. Hsu, R. Rujkorakarn, J. R. Sites, and C. Y. She, J. Appl. Phys. **59**, 3475 (1986).
[18] T. Nakayama, J. Electrochem. Soc. **141**, 237 (1994).
[19] R.-Y. Tasi and M.-Y. Hua, Appl. Opt. **35**, 5073 (1996).
[20] H. Nozoye and N. Nishimiya, Appl. Phys. Lett. **54**, 231 (1989).
[21] J. D. DeLoach and C. R. Aita, J. Vac. Sci. Technol. A **16**, 1963 (1998).
[22] M. D. Wiggins, M. C. Nelson, and C. R. Aita, J. Vac. Sci. Technol. A **14**, 772 (1996); Proc. Mat. Res. Soc. **398**, 381 (1996).
[23] P. Alexandrov, J. Koprinarova, and D. Todorov, Vacuum **47**, 1333 (1996).
[24] D. Wicaksana, A. Kobayashi, and A. Kinbara, J. Vac. Sci. Technol. A **10**, 1479 (1992).
[25] D. Guerin and S. Ismat Shah, J. Vac. Sci. Technol. A **15**, 712 (1997).
[26] M. G. Krishna, N. Rao, and S. Mohan, J. Appl. Phys. **73**, 434 (1993).
[27] L. M. Williams and D. W. Hess, J. Vac. Sci. Technol. A **1**, 1810 (1983).
[28] N. Martin, C. Rousselot, D. Rondot, F. Palmiro, and R. Mercier, Thin Solid Films **3000**, 113 (1997).
[29] J. D. DeLoach, G. Scarel, and C. R. Aita, J. Appl. Phys. **85**, 2377 (1999).
[30] J. A. Eastman, J. Appl. Phys. **75**, 770 (1994).
[31] V. V. Yakovlev, G. Scarel, C. R. Aita, and S. Mochizuki, Appl. Phys. Lett. **76**, 1107 (2000).
[32] J. Tauc, in *Amorphous and Liquid Semiconductors*, edited by J. Tauc (Plenum, London, 1974), Chap. 4.
[33] P. M. A. Sherwood, *Vibrational Spectroscopy Of Solids* (Cambridge University Press, Cambridge, UK, 1972).
[34] D. W. Berreman, Phys. Rev. **130**, 2193 (1963).
[35] F. L. Galeener and G. Lucovsky, Phys. Rev. Lett. **37**, 1474 (1976).
[36] F. L. Galeener, A. J. Leadbetter, and M. W. Stringfellow, Phys. Rev. B **27**, 1052 (1983).
[37] S. E. de Leeuw and M. F. Thorpe, Phys. Rev. Lett. **55**, 2879 (1985).
[38] M. F. Thorpe and S. E. de Leeuw, Phys. Rev. B **33**, 8490 (1986).
[39] J. M. Gales, B. Boltjes, M. F. Thorpe, and S. E. de Leeuw, Phys. Rev. B **40**, 7214 (1989).
[40] R. M. Almeida, Phys. Rev. B **45**, 161 (1992).
[41] E. I. Kamitsos, A. P. Patsis, and G. Kordas, Phys. Rev. B **48**, 12499 (1993).
[42] M. A. Ovchinnikov and C. A. Wight, J. Chem. Phys. **99**, 3374 (1993); **100**, 972 (1994); **102**, 67 (1995).
[43] R. J. Gonzalez, R. Zallen, and H. Berger, Phys. Rev. B **55**, 7014 (1997).
[44] See for example: H. P. Klug and L. E. Alexander, *X-Ray Diffraction Processes* (Wiley, New York, 1974).
[45] W. N. Hansen, J. Opt. Soc. Am. **58**, 380 (1968).
[46] Anatase: ASTM JCPDS File No. 21-1272 (1991).
[47] Rutile: ASTM JCPDS File No. 21-1276 (1991).
[48] B. L. Averbach and M. Cohen, Trans. AIME **176**, 401 (1948).
[49] L. S. Zevin and G. Kimmel, *Quantitative X-ray Diffractometry* (Springer, New York, 1995), pp. 188–204.

[50] M. Ocana, J. V. Garcia-Ramos, and C. J. Serna, J. Am. Ceram. Soc. **75**, 2010 (1992).
[51] B. C. Trasferetti, C. U. Davanzo, N. C. da Cruz, and M. A. B. de Moraes, Appl. Spectrosc. **54**, 687 (2000).
[52] D. M. Eagles, J. Phys. Chem. Solids **25**, 1243 (1964).
[53] A. Aoki, H. Tanaka, and K. Hisano, *Proceedings of the Twelfth Japan Symposium on Thermophysical Properties*, **A103** (1991), p. 9.
[54] N. W. Ashcroft and N. D. Mermin, *Solid State Physics* (Saunders College Press, Philadelphia, 1976).
[55] R. Fuchs, K. L. Kliewer, and W. J. Pardee, Phys. Rev. **150**, 589 (1966).
[56] R. G. Greenler, J. Chem. Phys. **44**, 310 (1966).
[57] R. Landauer, in *Electrical Transport and Optical Properties of Inhomogeous Media* edited by J. C. Garland and D. B. Tanner (American Institute of Physics, New York, 1978), p. 2.
[58] R. W. Cohen, G. D. Cody, M. D. Coutts, and B. Abeles, Phys. Rev. B **8**, 3689 (1973).
[59] D. Stroud, Phys. Rev. B **12**, 3368 (1975).
[60] R. Landauer, *op. cit.*, p. 10 (see Eqs. 3.5–3.7).